Influence of disorder on the vertical transport in wide barrier superlattices

H. Willenberg,* O. Wolst, R. Elpelt, W. Geißelbrecht, S. Malzer, and G. H. Döhler
Institut für Technische Physik I, Universität Erlangen, Erwin-Rommel-Strasse 1, Erlangen, Germany
(Received 23 April 2001; published 3 January 2002)

We report a combined theoretical and experimental study of vertical electron transport in wide barrier superlattices. The proposed microscopic transport model is applied to a parabolic $Al_{0.4}Ga_{0.6}As/GaAs$ structure and to a δ-doped GaAs superlattice. Taking into account the structure-dependent deviations from the ideal case, i.e., interface roughness in the first case and doping-induced disorder in the second case, we obtain quantitative agreement between calculated and measured current-voltage characteristics for both superstructures. While negative differential conductivity persists up to intermediate temperatures in the parabolic sample, the doping superlattice exhibits no fine structure of the current-voltage characteristics even at low temperatures. These findings are explained by comparing the inhomogeneous broadening of electronic states due to interface roughness (~ 10 meV) and doping-induced disorder ($\gtrsim 50$ meV). An analysis of photoluminescence spectra and current-voltage characteristics of the doping superlattice is used as an additional tool to verify the structure parameters, i.e., doping densities and period.

DOI: 10.1103/PhysRevB.65.035328 PACS number(s): 73.21.Cd, 72.80.Ng

I. INTRODUCTION

Vertical transport in semiconductor superlattices has been extensively studied both theoretically[1,2] and experimentally.[3,4] It is found that at sufficiently low fields the transport is confined to the lowest miniband (intraminiband transport). Negative differential conductivity (NDC) occurs if with increasing electric field F the (angular) frequency of the Bloch oscillations $\omega_B = eFd/\hbar$ exceeds the scattering rate $1/\tau$. The originally proposed semiclassical transport model[1] and its extensions[5–7] have to be replaced by a quantum-mechanical hopping model[2,8] at higher fields if the potential drop across a period of the superlattice, eFd, exceeds the miniband width Δ. The minibands transform into the Wannier-Stark ladder with a spacing of the energy levels eFd between neighboring wells. In this regime NDC persists, although resonant peaks of the current may occur due to enhanced LO phonon emission at $eFd = \hbar\omega_0$. At still higher fields the transport due to transitions from the lowest into higher minibands (interminiband transport) becomes possible if Wannier-Stark levels of the lowest miniband become resonant with those of a higher miniband in the neighboring well. This contribution produces additional current peaks, followed by regions of NDC.

In most of the cases reported in the literature the superlattices consisted of a sequence of rectangular quantum wells, which were more or less strongly coupled, depending on the thickness of the barriers. Whereas in strongly coupled superlattices the miniband width Δ is comparable with the gaps between minibands or even larger, in weakly coupled superlattices Δ amounts usually only to a few meV or even less. There has, however, been hardly any study of transport in ''ultraweakly coupled'' superlattices, in which the quantum wells are separated by wide barriers (''wide barrier superlattices,'' or WBSL's). The most prominent example of WBSL's are the *n-i-p-i* doping structures[9] with barrier heights typically comparable with the band gap and barrier widths typically exceeding 20 nm. A simple estimate shows that the current density may still be 1 mA/cm^2, or even larger, if the carrier density in the wells and the transition probability between adjacent wells exceed $n^{(2)} = 10^{12}$ cm^{-2} and $w = 6\times 10^3$ s^{-1} per carrier, respectively. The maximum drift velocity of the carriers at 1 mA/cm^2 would be only 10^{-2} cm/s for $d = 16$ nm, for example. This low drift velocity would, formally, correspond to an extremely small miniband width $\Delta = 2\hbar w \sim 10^{-8}$ meV according to the Esaki-Tsu model.

Obviously, the semiclassical picture of superlattice transport in terms of electrons performing Bloch oscillations fails for such narrow minibands for any reasonable field, as $eFd \gg \Delta$. But also the quantum-mechanical approach of calculating the transport in terms of hopping between the rungs of the Wannier-Stark ladder has to be modified for a realistic calculation of the transport as it does not take into account the fact that at the fields of interest the field dependence of the matrix elements for the hopping transitions are no longer correctly described by the Wannier-Stark states.

The most stringent shortcoming of the conventional superlattice transport theories, however, results from the fact that the effects of disorder are huge in WBSL's. They lead to an inhomogeneous broadening of the subband energies which strongly exceeds the miniband width Δ. As the lateral potential fluctuations are uncorrelated in neighboring quantum wells (QW's), this inhomogeneous broadening strongly influences the interlayer transitions of the electrons. The effect is particularly drastic for the ''intraminiband'' transport. The conventional transport models would predict an extremely sharp drop of the intraminiband current if the levels of the neighboring QW's get misaligned by a potential drop $eFd > \Delta$. Due to the inhomogeneous broadening of the subband states there is now a wide range of electric fields for which some of the energy levels of the adjacent wells get just aligned by the potential drop eFd. Later on we will see that these transitions allow for elastic tunneling or quasielastic phonon-assisted transitions, which are the origin of the low-field current in these WBSL's. Of course, peaks of the superlattice current are expected due to ''interminiband'' transitions, if the potential drop eFd between adjacent potential

wells corresponds to the energy difference between subbands. Whether these current peaks will be obscured by the disorder effects depends on whether the subband broadening is strong or weak compared to the subband spacing.

In this paper we develop and evaluate in Sec. II a realistic theoretical model for the calculation of transport in WBSL's, taking into account tunneling and phonon-assisted transitions between adjacent QW's, but still completely neglecting disorder. In Sec. III the influence of disorder is included by using suitable averaging procedures. We treat explicitly two interesting examples and compare the results with experiments. The first WBSL consists of a sequence of parabolic QW's (grown by the ''digital alloy'' technique[10]). This structure is particularly suitable for the observation of resonances in the current-voltage curves. Current peaks are expected each time the eFd amounts to a multiple of the harmonic-oscillator energy $\hbar\omega$ of the parabolic QW's. The disorder in these WBSL's can be modeled for the ''digital alloy'' technique. It turns out that the broadening due to disorder can be less than $\hbar\omega$ and current peaks are both expected and, in fact, experimentally observed. The second example of a WBSL is a δ-*n*-*i*-*p*-*i* superlattice. In this case the potential fluctuations originate from the random distribution of the ionized donors and acceptors within the *n*- and *p*-doping planes. They turn out to be very large. As a consequence we find, both theoretically and experimentally, that the disorder completely obscures the current peaks which would be expected in the absence of disorder.

In principle, the sequential tunneling model[11] is appropriate for describing electron transport in wide barrier superlattices for arbitrary fields. However, the inclusion of disorder effects is more easily performed in the model proposed in the following.

II. THEORY OF TRANSPORT IN AN IDEAL WEAKLY COUPLED SUPERLATTICE

We assume a superlattice with period d consisting of N barriers and $N-1$ potential wells, embedded between two *n*-doped contact layers. The shape of the potential could be arbitrary, but in the following we will consider explicitly only triangular (shown in Fig. 1) and parabolic potential wells. Furthermore we assume a constant electron density $n^{(2)}$ to be present in each potential well. In the case of the δ-doped *n*-*i*-*p*-*i* structure $n^{(2)}$ is given by the difference between the doping densities $n_D^{(2)}$ and $n_A^{(2)}$ in the *n* and *p* layers, respectively,

$$n^{(2)}=n_D^{(2)}-n_A^{(2)}.$$

In the parabolic wells it can be due to a weak uniform *n*-background doping, for example. Finally, we assume that the potential drop due to an applied voltage U is distributed uniformly across the superlattice, resulting in a uniform (external) field $F=U/Nd$, from which a potential drop per period of $eFd=eU/N$ follows (we neglect space-charge effects in the contact layers). The continuity condition for dc transport requires that the current between any two neighboring quantum wells of the structure will be the same. Therefore, it will be sufficient to evaluate the current density through a single barrier from left to right for a suitably defined double quantum well (DQW), as shown in Fig. 1 for the case of triangular wells.

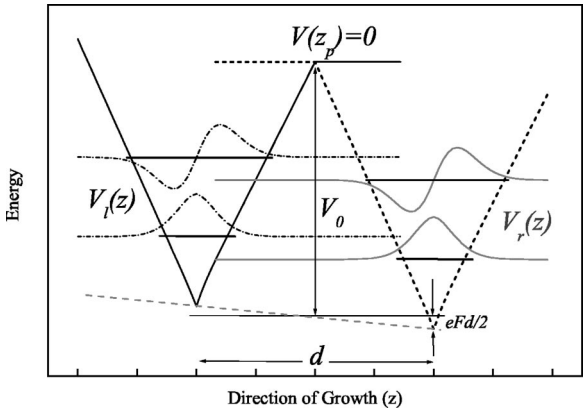

FIG. 1. The DQW potential in the presence of an external potential eFz (dashed line). The minima of the left (full line) and the right (dotted line) QW are shifted up or down, respectively, by an amount of $eFd/2$. For sufficiently low fields this applies also to the energies of the subband edges, $E_{\xi,n}$. It should be noted that each QW is defined on the entire Hilbert space [with $V_l(z)=0$ for $z>0$ and $V_r(z)=0$ for $z<0$]. The same is true for the corresponding wave functions.

A. Electronic states

The potential operator of the total two-well system can be split into three parts: a contribution from each of the QW's, labeled $V_{\xi=l,r}$ for left and right (see Fig. 1), and an additional interaction term $V_{ph}=V_{ph}^{LA}+V_{ph}^{LO}$ containing the contribution of acoustical- and optical-phonon processes, i.e.,

$$V(\mathbf{r},z,t)=V_l(z)+V_r(z)+V_{ph}(\mathbf{r},z,t). \tag{1}$$

A reasonable set of basis functions $\phi_{\xi n\mathbf{k}}(\mathbf{r},z)$ is formed by the bound eigenfunctions of the unperturbed single QW's, $\psi_{\xi n}(z)$ (calculated within the envelope function formalism), times plane waves corresponding to the free motion parallel to the layers:

$$\phi_{\xi n\mathbf{k}}(\mathbf{r},z)=\langle\mathbf{r},z|\xi n\mathbf{k}\rangle=\psi_{\xi n}(z)\cdot e^{i\mathbf{kr}}. \tag{2}$$

Note that only the wave functions $\psi_{\xi n}(z)$ of the same QW are orthogonal to each other, whereas any two wave functions belonging to different QW's have a finite (though typically very small) overlap. This overlap is responsible for the possibility of transitions between the left and right QW. For the states $|ln\mathbf{k}\rangle$ the potential $V_r(z)$ represents a perturbation and, vice versa, $V_l(z)$ for $|rn\mathbf{k}\rangle$. Thus, this choice of $V(\mathbf{r},z,t)$ yields in the solution of the Schrödinger equation both (momentum-conserving) tunneling terms of the type

$$\langle rm\mathbf{k}'|V_t|ln\mathbf{k}\rangle=\langle rm|V_t|ln\rangle\delta_{\mathbf{k},\mathbf{k}},$$

which contain the static potential of the neighboring wells [here $V_t=V_r(z)$] and time-dependent terms of the type

$$\langle rm\mathbf{k}'|V_q^{ph}e^{i\mathbf{qr}}|ln\mathbf{k}\rangle=\langle rm|V_q^{ph}e^{iq_zz}|ln\rangle\delta_{\mathbf{k}-\mathbf{k}'+\mathbf{q}_\parallel},$$

originating from the electron-phonon interaction, where V_q^{ph} denotes the Fourier component of the electron-phonon interaction potential corresponding to the momentum transfer $\mathbf{q}$ involved in the transition.

The probability amplitudes for the first-order transitions, $a_{li\mathbf{k}\to rf\mathbf{k}'}(V_\mu)$, or second-order transitions, $a_{li\mathbf{k}\to rf\mathbf{k}'}(V_\mu,V_\nu)$, for an electron crossing the barrier from an initial subband state on the left $|li\mathbf{k}\rangle$ to a final state at the right $|rf\mathbf{k}'\rangle$ via the interaction processes μ or μ,ν are evaluated using time-dependent perturbation theory. The transition rate up to second-order perturbation theory becomes

$$w_{li\mathbf{k}\to rf\mathbf{k}'}=\left|\sum_{\mu\nu} a_{li\mathbf{k}\to rf\mathbf{k}'}(V_\mu)+a_{li\mathbf{k}\to rf\mathbf{k}'}(V_\mu,V_\nu)\right|^2$$

$$\approx\sum_{\mu}\underbrace{|a_{li\mathbf{k}\to rf\mathbf{k}'}(V_\mu)|^2}_{\equiv w_{li\mathbf{k}\to rf\mathbf{k}'}(V_\mu)}$$

$$+\sum_{\mu\nu}\underbrace{|a_{li\mathbf{k}\to rf\mathbf{k}'}(V_\mu,V_\nu)|^2}_{\equiv w_{li\mathbf{k}\to rf\mathbf{k}'}(V_\mu,V_\nu)}, \tag{3}$$

where V_μ denotes the various interaction (tunneling or phonon) potentials involved in the transition. For the sake of simplicity, the interference terms between different paths from a given initial to a final state are neglected. Proofing that most of these contributions are ruled out because of energy and momentum conservation is straightforward, but fairly tedious.

The current density $\vec{j}$ is obtained by multiplying $w_{li\mathbf{k}\to rf\mathbf{k}'}$ with the occupation probability of the initial state, $f_{li\mathbf{k}}$, the probability of finding the final state empty $(1-f_{rf\mathbf{k}'})$, and subsequent summing over all initial and final states:

$$\vec{j}=e\sum_{i\mathbf{k}}\sum_{f\mathbf{k}'} f_{li\mathbf{k}}(1-f_{rf\mathbf{k}'})w_{li\mathbf{k}\to rf\mathbf{k}'}\,. \tag{4}$$

Similarly, the opposite current, $\overleftarrow{j}$, is expressed as

$$\overleftarrow{j}=e\sum_{f\mathbf{k}'}\sum_{i\mathbf{k}} f_{rf\mathbf{k}'}(1-f_{li\mathbf{k}})w_{rf\mathbf{k}'\to li\mathbf{k}} \tag{5}$$

and $j=\vec{j}-\overleftarrow{j}$ gives the total current. Here, $f_{li\mathbf{k}}$ and $f_{rf\mathbf{k}'}$ can be expressed by the equilibrium distribution

$$f_{\xi n\mathbf{k}}=\left\{\exp\left[\left(E_{\xi n}+\frac{\hbar^2\mathbf{k}^2}{2m^*}-\Phi_\xi\right)\Big/\,kT\right]+1\right\}^{-1}. \tag{6}$$

Note that the translational symmetry of the system results in $E_{rn\mathbf{k}}=E_{ln\mathbf{k}}-eFd$. The continuity condition for the current, in turn, requires

$$n_r^{(2)}=\sum_m\int\frac{d^2\mathbf{k}'}{(2\pi)^2}f_{rm\mathbf{k}'}=\sum_n\int\frac{d^2\mathbf{k}}{(2\pi)^2}f_{ln\mathbf{k}}=n_l^{(2)},$$

from which $\Phi_r=\Phi_l-eFd$ follows.

B. Transport mechanism

The evaluation of the probability rates of first and second order is complicated by the fact that the states forming the basis are neither orthogonal nor complete. In principle, the influence of the nonorthogonality could be corrected by a matrix inversion that decouples the probability amplitudes. The implications of nonorthogonal basis states in a two-well system were discussed in more detail by Prengel *et al.*[12] Here, its consideration leads to small corrections,[13] which are neglected in the following. The bound states are complemented by continuum states, taken as three-dimensional plane waves, to approximate a complete set of basis functions.

Another modification arises from the nonparabolic dispersion relations, which is taken into account by an energy-dependent effective mass within the barrier according to the increasing influence of the valence band (light holes) onto the states in the conduction band:[13]

$$m(E_z,z)\approx m^*\left(1-\theta[V(z)-E_z]\frac{V(z)-E_z}{E_g}\right), \tag{7}$$

where E_g is the band gap of the bulk material.

Tunneling has to be treated differently in a perturbation series: because of tunneling between two bound states being an intrinsically oscillating process, there is no contribution from the first-order tunneling terms nor from any term of higher order containing only energy- and momentum-conserving processes. Higher-order terms involving scattering and tunneling have to be corrected by a term $\eta=(1+\tau_s/\tau_t)^{-1}$ which compares time scales of the intrawell scattering process τ_s with that of the tunnel oscillation τ_t. This term essentially suppresses the Lorentzian sidebands of the resonant tunneling transition.

The first-order intrawell transition rate ($\xi'=\xi$) and interwell transition rate ($\xi'\neq\xi$) via acoustical- or optical-phonon scattering is obtained using Fermi's golden rule:

$$w_{\xi i\mathbf{k}\to\xi' f\mathbf{k}'}(V_{ph})=\frac{2\pi}{\hbar}\sum_{\mathbf{q}}|\langle\xi' f|V_q e^{\pm iq_z z}|\xi i\rangle|^2$$

$$\times\left(n_q+\frac{1}{2}\pm\frac{1}{2}\right)\delta_{\mathbf{k}-\mathbf{k}'\pm\mathbf{q}_\parallel}$$

$$\times\delta(E_{\xi' f\mathbf{k}'}-E_{\xi i\mathbf{k}}\pm\hbar\omega_q), \tag{8}$$

where $q=|\mathbf{q}|=\sqrt{\mathbf{q}_\parallel^2+q_z^2}$ and $n_q=[\exp(\hbar\omega_q/kT)-1]^{-1}$ is the occupation number of phonons according to the Bose-Einstein statistics; the upper sign corresponds to the emission of phonons. In the usual approximation, we take bulk phonon modes and the dispersion $\hbar\omega_q^{LA}=\hbar c_s q$ for acoustical phonons and $\hbar\omega_q^{LO}=\hbar\omega_0\approx 36$ meV for optical phonons. V_q depends on the type of phonons considered:[14]

$$V_q^{LA}=\sqrt{\frac{D_A^2\hbar}{2\rho c_s}q}, \tag{9}$$

where D_A denotes the deformation potential of acoustical phonons, ρ the mass density, and c_s the velocity of sound in the medium. For longitudinal optical phonons we use the Fröhlich interaction:[14]

$$V_q^{LO} = i\sqrt{\frac{e^2\hbar\omega_0}{2}\left(\frac{1}{\epsilon_\infty}-\frac{1}{\epsilon}\right)}\frac{q}{q^2+q_0^2}, \tag{10}$$

where $\epsilon, \epsilon_\infty$ are the low- and high-frequency dielectric constants, $\hbar\omega_0$ is the optical-phonon energy, and q_0 is the reciprocal screening length.

From the matrix elements in Eq. (8) it is evident that the interwell transition rates ($\xi' \neq \xi$), which contribute directly to the transport, are typically by many orders of magnitude smaller than the intrawell transition rates ($\xi' = \xi$). The latter ones contribute to transport only indirectly but they are very essential. They allow for inelastic intrawell scattering and, thus, for energy relaxation processes with a scattering rate $1/\tau_s$. Only these processes make tunneling between bound states possible, as mentioned before.

Compared to the first-order contribution, the second-order scattering process by two phonons of arbitrary type is negligible. The second-order phonon-assisted tunneling processes turn out to be the dominant contribution to the transport ($\xi' \neq \xi$):

$$w_{\xi i\mathbf{k}\to\xi' f\mathbf{k}'}(V_t, V_{ph}) = \frac{2\pi}{\hbar}\sum_{\mathbf{q}} \delta(E_{\xi' f\mathbf{k}'} - E_{\xi i\mathbf{k}} \pm \hbar\omega_q) \times \left| \sum_{\xi'' n\mathbf{k}''} \frac{\langle \xi' f\mathbf{k}'|V_q e^{\pm iq_z z}|\xi'' n\mathbf{k}''\rangle\langle \xi'' n\mathbf{k}''|V_{\bar{\xi}}|\xi i\mathbf{k}\rangle}{E_{\xi i\mathbf{k}} - E_{\xi'' n\mathbf{k}''} + i\Gamma}\right|^2. \tag{11}$$

Here, the broadening parameter Γ expresses the fact that the intermediate states $|\xi'' n\mathbf{k}''\rangle$ exhibit a finite lifetime, which in turn is roughly given by the first-order intrawell phonon-scattering time τ_s, which takes place between two subbands of either the left or the right QW.

In our case the summation over all intermediate states $|\xi'' n\mathbf{k}''\rangle$ in Eq. (11), which usually represents a major problem when evaluating second-order matrix elements, is largely reduced by the fact that the number of allowed intermediate states is reduced to a few, energetically well-separated terms due to the $\mathbf{k}$ conservation required for the tunneling process.

$$w_{\xi i\mathbf{k}\to\xi' f\mathbf{k}'}(V_t, V_{ph}) = \frac{2\pi}{\hbar}\sum_{\mathbf{q}}\sum_{\xi'' n\mathbf{k}''} \left| \frac{\langle \xi' f|V_q e^{\pm iq_z z}|\xi'' n\rangle\langle \xi'' n|V_{\bar{\xi}}|\xi i\rangle}{E_{\xi i\mathbf{k}} - E_{\xi'' n\mathbf{k}''} + i\Gamma}\right|^2 \times \delta_{\mathbf{k}''-\mathbf{k}'\pm\mathbf{q}_\parallel}\delta_{\mathbf{k}-\mathbf{k}''}\delta(E_{\xi' f\mathbf{k}'} - E_{\xi i\mathbf{k}} \pm \hbar\omega_q). \tag{12}$$

Obviously, tunneling takes place between different wells, which gives $\xi'' \neq \xi$, and relaxation is dominated by intrawell phonon scattering, which yields $\xi' = \xi''$. After further evaluation of Eq. (12) and summation over all final states, the second-order transition rate of crossing the barrier from the initial state $|\xi i\mathbf{k}\rangle$ to any state of the other well $\bar{\xi}$ becomes

$$w_{\xi i\mathbf{k}}(V_t, V_{ph}) = \sum_n \underbrace{\frac{1}{\tau_{i,n\mathbf{k}}}}_{\text{relaxation}} \underbrace{\frac{|\langle \bar{\xi} n|V_{\bar{\xi}}|\xi i\rangle|^2}{(E_{\xi i} - E_{\bar{\xi} n})^2 + (\hbar/\tau_{i,n\mathbf{k}})^2}}_{\text{resonant tunneling}}, \tag{13}$$

where $1/\tau_{i,n\mathbf{k}}$ (corresponding to the unspecified quantity $1/\tau_s$ in the discussion above) is the intrawell scattering rate from the virtual intermediate state to all unoccupied final states. Thereby, we set $\Gamma \approx \hbar/\tau_{i,n\mathbf{k}}$, which becomes strictly accurate in the resonant situation, $E_{\xi i} = E_{\bar{\xi} n}$, the case of the largest contribution.

In order to account for the contribution of carriers thermally activated into continuum states (i.e., $E_z > 0$), the model is extended to allow for charge transport carried by three-dimensional states. Thermally activated hopping is given by

$$j^{th}_{\xi\to\bar{\xi}}(F) = e\sum_{k_z,\mathbf{k}} \nu_\xi(k_z) f_{\xi k_z\mathbf{k}}(1 - f_{\bar{\xi} k_z\mathbf{k}}), \tag{14}$$

where $\nu_\xi(k_z) = v_z/2d$ denotes the classical frequency associated with the group velocity $v_z = \hbar k_z/m^*$, which is related to the z component of the kinetic energy (with respect to the bottom of the well) by

$$k_z = \sqrt{2m^*(E_z + V_0 \mp eFd/2)/\hbar}, \tag{15}$$

where the upper/lower sign corresponds to the left/right well. At high fields the occupation factor of final states $f_{\bar{\xi} k_z\mathbf{k}}$ is negligible, whereas it is compensated by the backward current at very low fields. Thus, we obtain a Richardson-like expression,

$$j^{th}_{\xi\to\bar{\xi}}(F) = \frac{em^*kT}{2\pi^2\hbar^3}\int_0^\infty dE_z \ln\left[1 + \exp\left(-\frac{E_z - \Phi_\xi}{kT}\right)\right]. \tag{16}$$

Note in this approximation the field dependence of the thermally activated current $j^{th}(F) = \vec{j} - \overleftarrow{j}$ is only due to the field dependence of Φ_l and Φ_r.

C. Results

Figure 2 shows a theoretical current-voltage characteristic of a perfect superlattice (SL) with nominal values $n_D^{(2)} = 4 \times 10^{12}$ cm^{-2}, $n_A^{(2)} = 3\times 10^{12}$ cm^{-2}, and $d = 40$ nm at a temperature $T = 4$ K. The contribution from first-order phonon scattering to perpendicular electron transport exhibits a steplike electric-field dependence. The steps correspond to the increase of available final states, whenever a subband edge on the right side is pulled below the chemical potential on the left. At elevated temperatures the steps vanish as the Fermi distribution function becomes smoother. As expected, the model predicts sharp peaks when two energy levels belonging to adjacent quantum wells are brought in resonance by an electric field corresponding to $eFd = \Delta E_{if}$, where ΔE_{if} is the energy difference between the initial and final

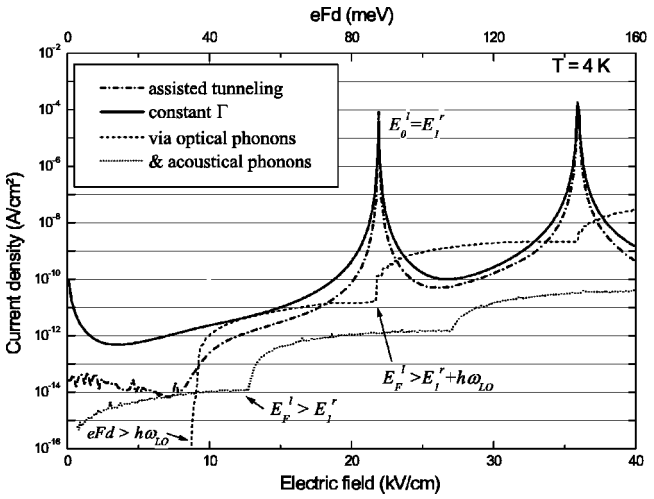

FIG. 2. Contributions to the ideal current-voltage characteristic of a wide barrier SL with triangular wells at low temperature ($T = 4$ K). The dominating second-order assisted tunneling process is considerably simplified by assuming a constant Γ for the intrawell scattering processes.

subbands *i* and *f*. The width of the resonance peaks is due to the finite lifetime of the levels caused by the interaction with acoustic- and optical-phonon modes. The broadening is well below 1 meV.

The calculation of the second-order tunneling process is accelerated by orders of magnitude by assuming a constant intrawell scattering time Γ. From Fig. 2 we see that the current density is overestimated for low fields ($eFd < \hbar\omega_0$). For higher energies, and in particular, close to the resonances, the agreement of both curves is satisfying. In terms of calculation time, this approximation is a prerequisite for the simulation of realistic structures exhibiting interface roughness or doping-induced disorder. In the following a constant scattering time is used in the evaluation of the tunneling current and the weak nonresonant background of phonon scattering will be neglected.

III. INFLUENCE OF DISORDER

In this section the theoretical model is applied to two different wide barrier superlattice structures with both a different shape of the quantum wells and a different origin of the disorder. The design of these superlattices corresponds closely to that of the structures experimentally investigated later on. In Sec. III A the parabolic potential for the electrons and the disorder is created by variation of composition in a digital alloy. In Sec. III B the quantum wells originate from the space-charge potentials in a δ-doped *n-i-p-i* superlattice and the disorder is due to the statistical distribution of the dopands within the doping layers. The specific disorder potentials are taken into account within the so-called local quantum-mechanical model similar to the one developed by Metzner *et al.*[15] for the case of luminescence in doping superlattices. In this model the assumption is being made that the three-dimensional fluctuating potential $V(\mathbf{r},z)$ changes slowly with regard to the lateral direction $\mathbf{r}$. Therefore, the subband states can still be expressed locally as a product of a *z*-dependent envelope function $\psi_{\xi,n}(z)$ and a plane wave $e^{i\mathbf{kr}}$. Consistent with these assumptions, the disorder can be taken into account by simply solving the one-dimensional Schrödinger equation for a sufficiently large number of points $\mathbf{r}$ (or for the central point $\mathbf{r}=0$ in a sufficiently large number of configurations). This results in a probability distribution $g_n(E)$ for the subband energies E_n and the corresponding envelope functions $\psi_n(z)$. For the calculation of transitions between different layers it is assumed that the probability distributions in different layers are uncorrelated, which appears to be a realistic assumption. In this model, the $\mathbf{k}$ vector is strictly preserved in tunneling processes, which is of tremendous help in performing transport calculations. One has, however, to bare in mind that this assumption becomes increasingly doubtful in the case of increasingly strong lateral disorder, where the in-plane part of the electron wave functions becomes strongly localized. Nevertheless, even for this case this model has provided excellent quantitative agreement between experiment and theory without any fitting parameter for the case of the luminescence spectra in *n-i-p-i* doping superlattices.[15] For the calculation of the current, a ($\mathbf{r}$-independent) ''global'' Fermi level $\Phi_\xi = \Phi_0 - \xi eFd$ is assumed for the ξth potential well. It is important to note that due to the uncorrelated spatial fluctuations, the alignment of *local* energy subbands $E_{\xi n}(\mathbf{r})$ and $E_{\xi+1 n}(\mathbf{r})$ is no longer a δ function of the electric field but it will occur with a certain probability at some field within a range of potential drops eFd which depends on the width of the distribution function $g_n(E)$. The probability of finding the initial state occupied and the final state empty, however, depends on the distance from the respective global Fermi levels. Averaging over all the local characteristics (or over all the configurations $\tilde{c}$) gives the macroscopic quantity, e.g., the current density: $j(F) = N^{-1}\Sigma_{\tilde{c}=1}^{N} j_{\tilde{c}}(F)$.

A. Interface roughness

We consider an $Al_xGa_{1-x}As/GaAs$ compositional superlattice with a periodic parabolic potential whose barrier height and period are similar to corresponding values of a typical doping superlattice. As we are interested in (unipolar) electron transport only, the contrary shape (opposite) modulation of the valence-band edge is of minor importance. The sample is assumed to be grown by the ''digital alloy'' technique.[10,16] The superlattice has a nominal period of 40 nm and consists of $Al_{0.4}Ga_{0.6}As$ barriers and GaAs wells with an underlying superlattice period of 2 nm and a parabolic variation of the barrier-to-well thickness ratio (see inset in Fig. 3).

The disorder effects in this structure are assumed to result only from interface roughness. In order to simulate this kind of disorder we allow for each period of the superlattice random fluctuations of the barrier thickness by ± 1 ML (at the dispense of the corresponding well width). In Fig. 4 the broadening of the energies E_n of the bottom of the subbands obtained from an evaluation of this model is depicted. In our calculations interface roughness gives rise to a quasi-Gaussian weak inhomogeneous broadening of about 10 meV,

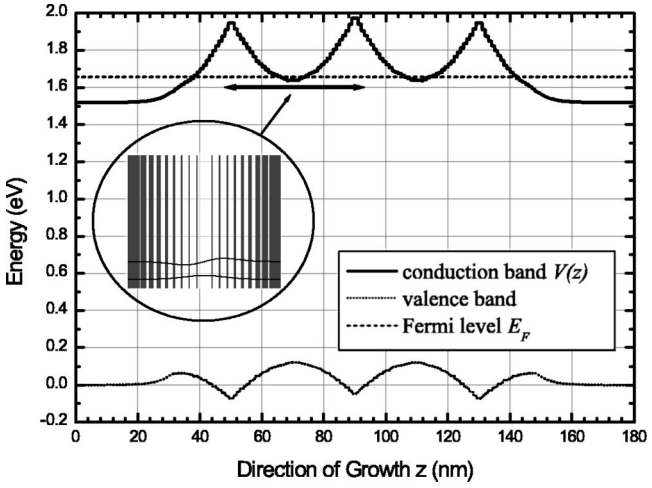

FIG. 3. Parabolic potential-well sample, $d=40$ nm, barrier height$=324$ MeV, grown by the digital alloy layer growth technique (the black stripes in the inset represent the $Al_{0.4}Ga_{0.6}As$ barriers and the white regions the GaAs wells. Two wave functions to the digital parabolic potential are shown.)

which is relatively small compared with the harmonic-oscillator energy spacing of 34 meV and in good accordance with literature.[17] In addition, the results do not show a subband-dependent broadening.

B. Doping-induced disorder

The real potential in a doping superlattice differs significantly from the (usually considered) averaged potential $V_j(z)$, obtained with uniformly distributed space charge of the dopands (''jellium model''[15]) because of the random distribution of the dopands on the corresponding lattice sites of the host material. This type of disorder is an intrinsic feature of the doping process itself and strongly influences optical and electrical properties[19] of *n-i-p-i* crystals.[9] According to Schubert *et al.*[20] δ-doped structures, with doping ideally restricted to one monolayer,[21] should exhibit minimal doping-induced disorder effects. In our simulations, the donor and acceptor doping atoms are assumed to be statistically distributed within the respective doping planes. In fact, ordering during the growth process, due to Coulomb repulsion of dopands,[22] generally does not seem to play a significant role. In Fig. 5 a cross section of the conduction-band edge, modulated by the space-charge potential $V(x,y,z)$ of a *p-i-n-i-p-i-n-i-p* structure, is shown for $y=y_0=$const (the first and the last *p* layer are assumed to be uniformly doped, whereas the dopands are randomly distributed in the *n* and the *p* layers). This figure is very instructive. First of all it depicts the strong and uncorrelated potential fluctuations close to the two donor layers. Here the potential fluctuations are partially screened by the mobile electron charge which resides preferentially in the regions of above-average donor density (''clusters''). Second, we see that the fluctuations of the height and shape of the potential barrier created by the (negatively charged) ionized acceptors are even more pronounced, as there are no holes in the *p* layers which could locally screen the acceptor space charge. Third, we see, with regard to the influence of the potential fluctuations on transport, that the regions with below-average acceptor density (''acceptor voids'') represent saddles of the potential mountains where tunneling is much more probable than on the average. Moreover, this has a particularly pronounced effect on thermally activated transport.[13]

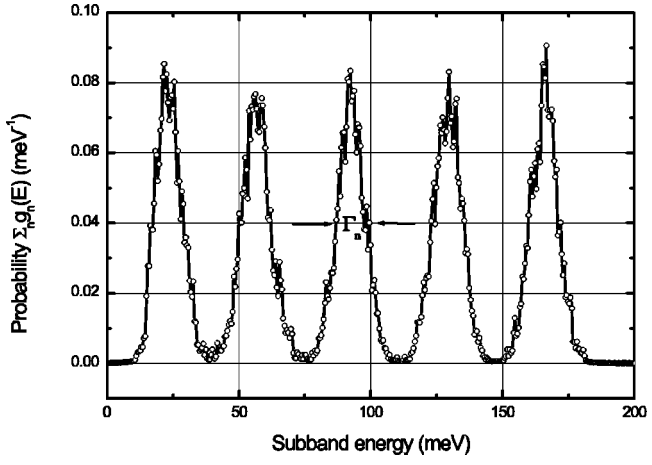

FIG. 4. The simulation of interface roughness of ± 1 ML results in random subband fluctuations of the energies E_n of the bottom of the subbands of about 10 meV. The broadening parameters Γ_n shows almost no dependence on the subband energy E_n.

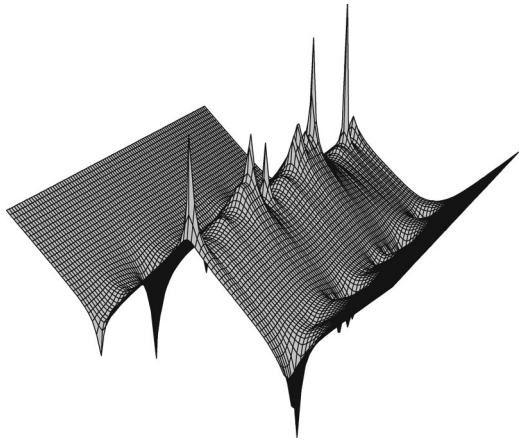

FIG. 5. Cross section of the conduction-band edge, modulated by the space-charge potential $V(x,y,z)$ of a *p-i-n-i-p-i-n-i-p* structure shown for $y=y0=$const (the first and the last *p* layer are assumed to be uniformly doped, whereas the dopands are randomly distributed in the *n* and the *p* layers. A cluster of doping atoms form sharp spikes and local voids form wide saddle points. The fluctuations in the range of 100 meV are comparable to or even exceed the subband energy differences.

As mentioned at the beginning of Sec. III, there are two methods to obtain the random potential. Instead of arranging the dopands on macroscopic layers as depicted in Fig. 5, in order to obtain quantitative results, it is numerically more efficient to distribute dopands on a large number of relatively small configurations (diameter ≈ 50 nm) and to compute a potential profile $V_{\tilde{c}}(z)$ along the central *z* axis (see Fig. 6) of each configuration.

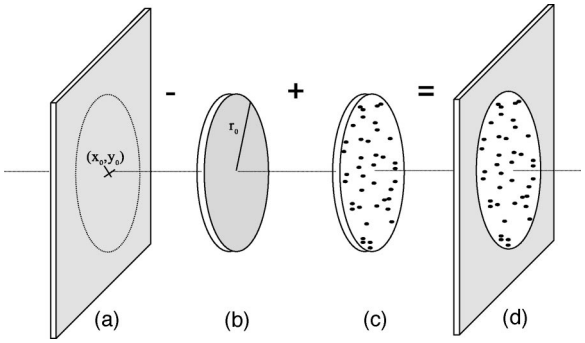

FIG. 6. Procedure to create the local potential profile for a specific configuration $V_{\tilde{c}}(z)$: (a) the (infinite) homogeneously charged doping layer provides the (average) jellium potential, (b) the average potential of a finite homogeneous circular disc (diameter ≈ 50 nm) is cut out and its contribution to the potential is subtracted, (c) the fluctuating potential due to a disc of the same diameter with randomly distributed dopands is inserted and its contribution to the potential $V_{\tilde{c}}(z)$ is added within the previous disc, and (d) the relevant charge distribution for the local potential profile is along the central z axis $V_{\tilde{c}}(z)$.

Screening effects of excess carriers in the n layers are taken into account by linear screening for the donors, using a Yukawa, instead of the Coulomb, potential. The potential of a single donor is then given by

$$V(R) = \frac{-e^2}{4\pi\epsilon\epsilon_0} \frac{e^{-R/L_s}}{|R|}, \tag{17}$$

where the screening length L_s is approximated by the isotropic Thomas-Fermi screening length at $T=0$ K:

$$L_s = \sqrt{\frac{\epsilon\epsilon_0 \pi\hbar^2}{e^2 m^*_{e,h}}} \left(\frac{\pi}{3n^{(3)}} \right)^{1/6}, \tag{18}$$

where $m^*_{e,h}$ is the averaged electron-hole mass.

Screening of the acceptor potential is achieved by a method based on mirror charges: it is well known that the electric field of an electric charge next to a metallic plane can be computed by assuming a mirror charge. We apply this idea to obtain a simple and fairly accurate description of screening effects of the ionized acceptor charges in the p layer by mobile electrons in the n layers. If the concentration of excess carriers in the n plane is sufficiently large to allow for a lateral displacement of electrons, the n layer can be approximated by a metallic plane. The screening of the charges in the p layer is then calculated by assuming a mirror $\overline{p}$ layer with equally distributed opposite charges in the distance d. As we have two n layers within our structure, we obtain an infinite arrangement of p and $\overline{p}$ layers. The potential of a single acceptor at $(\mathbf{r},z=0)$ is then written as

$$V(\mathbf{r},z) = \frac{e^2}{4\pi\epsilon\epsilon_0} \sum_{n=-\infty}^{\infty} \frac{(-1)^n}{\sqrt{\mathbf{r}^2 + (z-nd)^2}}, \tag{19}$$

where n denotes the order of mirror planes considered. The potential series rapidly converges and ten orders turn out to be sufficient. From the random distribution of dopands and the subsequent computation of screened potentials, we extract a large number of potential profiles (configurations $\tilde{c}$).

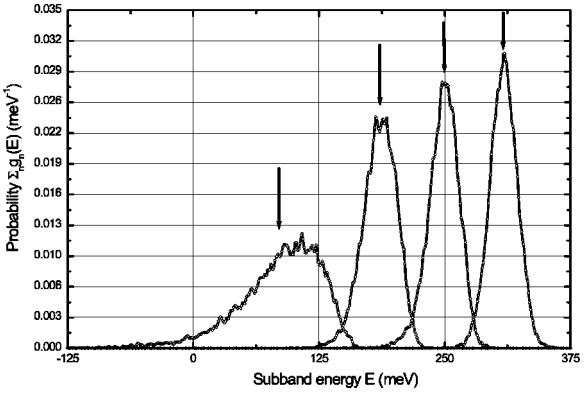

FIG. 7. The local subband shows fluctuations of several tens of meV. The arrows indicate the subband energy without disorder. In contrast to the previous situation of the parabolic structure, the subbands are not well separated. Other features of this type of disorder are the increased broadening of low subbands and the asymmetric shape of the probability functions corresponding to the localization of electrons.

Figure 7 is the homologue to Fig. 4 for the subband-edge energies in the case of doping-induced disorder for the n layer of a δ-doped superlattice with nominal values $n_D^{(2)} = 4 \times 10^{12}$ cm^{-2}, $n_A^{(2)} = 3 \times 10^{12}$ cm^{-2}, and $d = 40$ nm. Obviously, the effect of disorder in a doping superlattice (DSL) is much more drastic compared to the previous case. In particular we note a very strong broadening of the lowest subband edge, which results from the fact that the wave function is strongly confined to a narrow region close to the center of the n layer where the potential $V_{\tilde{c}}(z)$ exhibits the largest fluctuations. These strong fluctuations are the physical reason why the effects of resonant tunneling will turn out to be completely obscured and NDC will not be observable even in measurements at low temperatures, where only the lowest subband is occupied.

C. Comparison with experiment

Current vs voltage measurements were performed at various temperatures between 16 and 300 K on mesa-shaped wide barrier superlattice samples with different superlattice design. Here we report on a sample with three parabolic $Al_{0.4}Ga_{0.6}As$ quantum wells and another one with 11 δ-n-i-p-i periods. The quantum well structures were imbedded between n-doped contact layers. A detailed description of the sample design, the molecular-beam epitaxy growth, and sample processing will be given elsewhere.[18]

Figure 8 shows theoretically calculated and measured I-V characteristics of the parabolic heterotype SL at low temperature, $T=16$ K. At this temperature, transport is essentially only due to tunneling. The theory is in good agreement with experiment, with respect to the exponential average increase of the current density, and the absolute values, as well as with regard to the peak positions. The Fermi level was used as a parameter in this special case of an undoped struc-

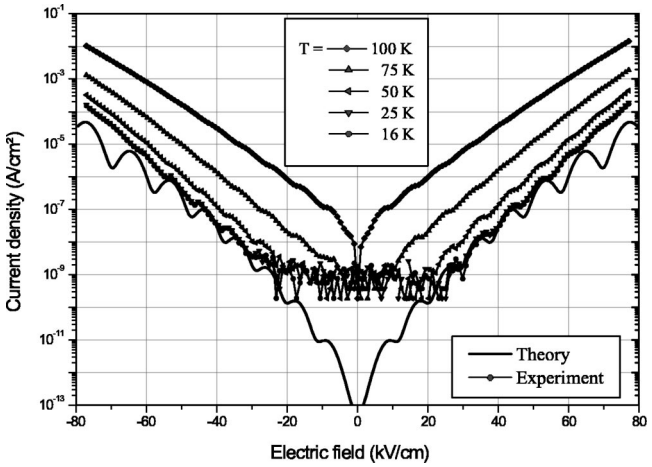

FIG. 8. Comparison of theoretical simulation and measurement of current density versus electric-field characteristics measured at a sample with three parabolic quantum wells at five different temperatures, as indicated, with a theoretical simulation for low temperature, $T=16$ K. The parabolic wells correspond to those of Sec. II A. Barrier height, given by the maximum aluminum content, and period of the structure enter the calculation. In this case the Fermi level was used as a parameter in this special case of an undoped structure.

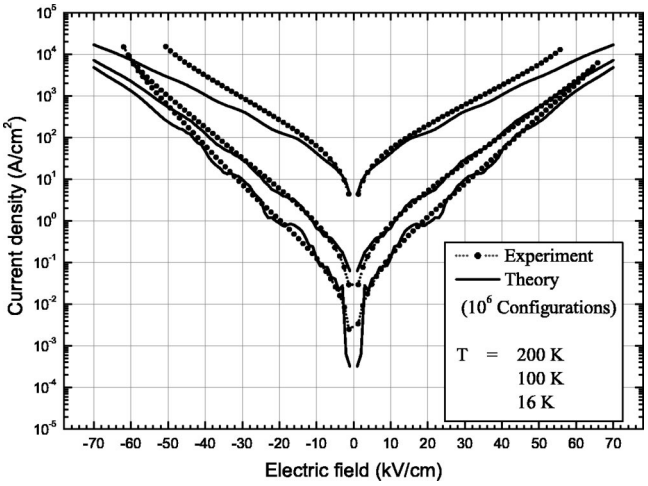

FIG. 9. Comparison between theoretical and experimental current density vs applied field characteristics for the temperatures 16 K, 100 K, and 200 K for a sample with 11 periods with $d=36.8$ nm, $n_D^{(2)}=7.2\times10^{12}$ cm^{-2}, and $n_A^{(2)}=3.35\times10^{12}$ cm^{-2}. The theoretical curves represent an average over 10^6 configurations. We observe excellent agreement between measured and calculated characteristics over a wide range of fields and temperatures. The resonant character of the tunneling process almost completely vanishes. Below about 50 kV/cm and 100 K tunneling represents the dominant transport mechanism. The deviations at high fields indicate field-induced electron heating. The assumption of a Fermi-Dirac distribution with the lattice temperature does not hold anymore.

ture. The resulting electron density $n^{(2)}=1\times10^{12}$ cm^{-2} in the inner parabolae implies only minor distortions of the total potential by space charges. The predicted resonant structure in the current density for $eFd=n\hbar\omega=n\times34$ meV is clearly reflected in the measurements. At low fields and low temperatures the subband structure cannot be detected as the currents are below the noise level of the pico-Amperemeter. Because of the approximately equidistant energy levels in the parabolic quantum wells the resonances, in particular those corresponding to low index n, are observed up to fairly high temperatures, $T=100$ K. Beyond this temperature unbound states take over the major contribution.

The deviations at higher fields as well as a less good agreement at elevated temperatures arise from the fact that the sample is undoped and the free-carrier density therefore depends on the injection current through the first barrier. In this case the assumption of a fixed Fermi level is no longer valid and a more rigorous treatment of this structure is needed to account for this effect.

Because of the triangular shape of the barriers, the theoretical current-voltage characteristics of DSL samples is extremely sensitive to small changes in the sample parameters, i.e., the period d and both donor and acceptor densities. Whereas d can be controlled quite accurately, the barrier height depends also on the less well-controlled doping densities. Therefore, we have determined the actual doping densities from a combined experimental and theoretical study of the strongly intensity-dependent luminescence spectra. By calculating the photoluminescence signal (see the Appendix) using the same approach for the electronic structure, including disorder effects, and with adjustable doping densities, we were able to find a set of doping parameters which only slightly differs from the nominal values but which provides agreement in accordance with both luminescence and transport experiments after a few iterations.

Figure 9 finally shows quantitative agreement of the theoretically calculated and the measured current density vs field characteristics of the 11-period DSL. For the calculations the design parameters resulting from the luminescence studies were used. No further parameters were adjusted. Therefore, the good agreement over many orders of magnitude and over a wide range of temperatures is quite remarkable. The fact that even the weak structure due to resonant tunneling which is still expected from the theory is not observed in the experiments indicates that the role of doping-induced disorder may even be larger than expected from our model.

IV. SUMMARY

In conclusion, we have investigated the influence of two different types of disorder, namely interface roughness and doping-induced fluctuations on vertical electron transport in weakly coupled SL's. Our results indicate that doping-induced disorder effects prevent the formation of negative differential conductivity in the n-type DSL, whereas interface roughness in a heterotype SL permits the observation of NDC. Accordingly, the inhomogeneous broadening is found to be much more pronounced in a DSL than in a heterotype SL, despite their similar conduction-band shape. While in the latter case interface roughness leads to values of about 10 meV, doping-induced disorder easily exceeds a 50 meV broadening of the confined states, though we chose the

δ-doped structure that is supposed to minimize disorder effects.

In addition, together with photoluminescence spectra, the results for DSL's allow the verification or calculation of nominal sample parameters and lead to a consistent picture of a vertical transport mechanism in the DSL. In a typical DSL the electronic transport is carried by tunneling transitions at fields up to 50 kV/cm and temperatures below 100 K. Beyond these limits thermally assisted hopping is found to be the dominant transport channel.

ACKNOWLEDGMENTS

We wish to thank S. Rott and C. Metzner for numerous stimulating discussions. This work was financially supported by the Deutsche Forschungsgemeinschaft.

APPENDIX: PHOTOLUMINESCENCE SPECTRA OF δ-DOPED GaAs SL's

Due to the triangular shape of the barriers the current-voltage characteristic of a DSL is very sensitive to the *p*-doping density, which determines the barrier height. In order to compare theoretical and experimental findings, it is necessary to verify the superlattice parameters, which enter the simulation, by means of additional measurements. We measured photoluminescence spectra and performed simulations, again within the local quantum-mechanical model, using the same set of doping parameters as were used for the *I* vs *V* characteristics.

Due to the spatial separation of the electron and hole wave functions, photon-excited carriers in DSL's exhibit a very long recombination lifetime (up to milliseconds). Thus, after an excitation of a laser pulse the electron and hole distributions are decoupled and relax independently towards thermal distributions within each conduction and valence band, which may be characterized by quasi-Fermi levels, Φ_n and Φ_p. The excitation level is defined by $\Delta\Phi_{np}=\Phi_n-\Phi_p$.

At low excitation a few electron-hole pairs will be created which hardly influence the space-charge potential. The resulting luminescence spectrum will therefore peak at the fundamental effective band-gap energy of the DSL, which de-

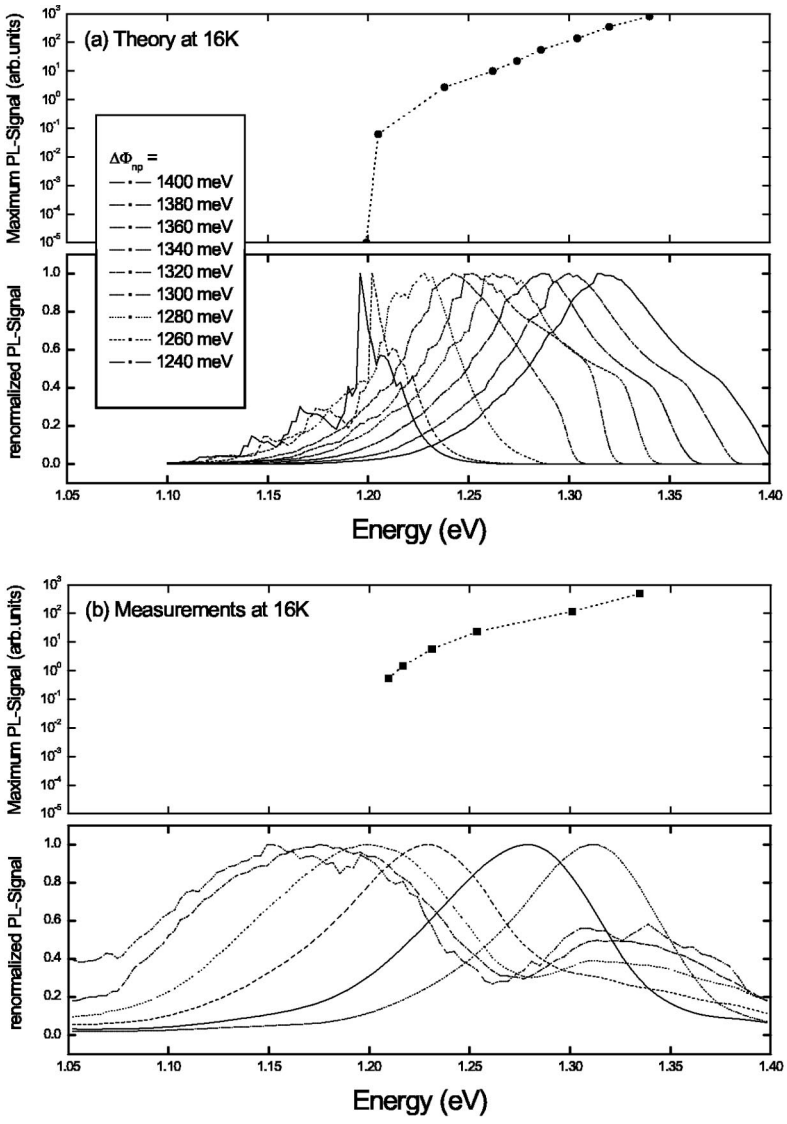

FIG. 10. Comparison of theoretical (a) and experimental (b) luminescence signals. The lower part shows the normalized spectra. The space-charge potential is screened by the excitation of free carriers and the effective band gap is thereby increased: the main peak moves to higher photon energies. Sweeping down to low excitation levels the peak saturates at the ground-state effective band-gap energy, which is shown in the upper part of both figures.

termines the dark current-voltage characteristic. The effective band gap directly gives the barrier height, from which the *p* doping is deduced. On the other hand, a highly excited DSL will eventually show the band gap of the bulk material, here GaAs, as the large density of electrons and holes completely screens the doping-induced space-charge potential.

To know whether the excitation level is sufficiently low to observe the ground-state effective band gap, a series is taken of spectra of varying excitation intensities. Starting from a value up to the band gap of GaAs, the peak of the spectra will redshift until it reaches the effective band gap, where its position remains nearly constant while the intensity drops due to the decreasing number of electron-hole pairs.

The lower graphs in Figs. 10(a) and 10(b) show the calculated and measured redshift, respectively, of the normalized luminescence signal with decreasing excitation, whereas the upper graphs depict the shift of the high-energy shoulder at a value of 80%. The photon energy, where the peak position remains nearly unchanged, corresponds to the effective band gap of the DSL. Due to the existence of tail states corresponding to potential spikes (compare Fig. 5) it is preferable to consider the high-energy shoulder of the spectra instead of the actual peak position.

In order to obtain the real sample parameters, the measured *I* vs *V* curves and the photoluminescence spectra are compared to their simulated counterparts. First, the *p* doping is adjusted until the experimental saturation energy is reproduced by the theoretical shift. Then, the period of the SL is optimized by adjusting the slope of the *I* vs *V* curves. Finally, the *n* doping gives the absolute value of the current density. After a few iterations a set of doping parameters is found in accordance with the experimental photoluminescence and measured electrical current densities.

The DSL investigated in this paper shows a good agreement of the upper graphs of Figs. 10(a) and 10(b) corresponding to theoretical and experimental values of the saturation energy as well as a quantitative agreement of the *I* vs *V* curves in Fig. 9 by using

$$d = 36.8 \text{ nm}, \quad n_D^{(2)} = 7.2 \times 10^{12} \text{ cm}^{-2},$$

$$n_A^{(2)} = 3.35 \times 10^{12} \text{ cm}^{-2}$$

instead of the nominal values

$$d = 40 \text{ nm}, \quad n_D^{(2)} = 4 \times 10^{12} \text{ cm}^{-2}, \quad n_A^{(2)} = 3 \times 10^{12} \text{ cm}^{-2}.$$

Apart from the significantly higher value for the *n* doping, which has only a minor effect on the height of the potential barrier, the deviations are only about 10%. However, due to the crucial influence of barrier height and period, the agreement between experiment and theory would be very poor (deviations by several orders of magnitude) if the (slightly different) nominal values for *d* and $n_A^{(2)}$ were used.

*Present address: Institut de Physique, Université de Neuchâtel, CH-2000 Neuchâtel, Switzerland.

[1] L. Esaki and R. Tsu, IBM J. Res. Dev. **14**, 61 (1970).
[2] R. Tsu and G.H. Döhler, Phys. Rev. B **12**, 680 (1975).
[3] F. Capasso, K. Mohammed, and A.Y. Cho, Appl. Phys. Lett. **48**(7), 478 (1986).
[4] A. Sibille, J.F. Palmier, H. Wang, and F. Mollot, Phys. Rev. Lett. **64**(1), 52 (1990).
[5] A.A. Ignatov and Yu.A. Romanov, Phys. Status Solidi B **73**, 327 (1976).
[6] P. Binder, S. Roth, and G. H. Döhler (unpublished).
[7] S. Rott, N. Linder, and G.H. Döhler, Physica B **272**, 213 (1999).
[8] S. Rott, P. Binder, N. Linder, and G.H. Döhler, Physica E (Amsterdam) **2**, 511 (1998).
[9] G.H. Döhler, Phys. Status Solidi B **52**, 79 (1972).
[10] A.C. Gossard, M. Sundaram, and P.F. Hopkins, in *Wide Graded Potential Wells in Semiconductors and Semimetals, Epitaxial Microstructures*, edited by R.K. Willardson, A.C. Beer, and E.R. Weber (Academic Press, New York, 1994), Vol. 40.
[11] A. Wacker, A.-P. Jauho, S. Zeuner, and S. J. Allen, Phys. Rev. B **56**, 13 268 (1997).
[12] F. Prengel, A. Wacker, and E. Schöll, Phys. Rev. B **50**, 1705 (1994).
[13] R. Elpelt, in *Physik Mikrostrukturierter Halbleiter*, edited by S. Malzer, T. Marek, and P. Kiesel (Lehrstuhl für Mikrocharakterisierung, Erlangen, Germany, 2000), Vol. 13.
[14] P.Y. Yu and M. Cardona, *Fundamentals of Semiconductors* (Springer, Berlin, 1996).
[15] C. Metzner, K. Schrüfer, U. Wieser, M. Luber, M. Kneissl, and G.H. Döhler, Phys. Rev. B **51**, 5106 (1995).
[16] W. Geißelbrecht, in *Physik Mikrostrukturierter Halbleiter*, edited by S. Malzer, T. Marek, and P. Kiesel (Lehrstuhl für Mikrocharakterisierung, Erlangen, Germany, 2000), Vol. 15.
[17] A. Thränhardt, J. Hader, and S.W. Koch, Phys. Rev. B **58**, 1512 (1998).
[18] R. Elpelt, O. Wolst, H. Willenberg, S. Malzer, and G. H. Döhler (unpublished).
[19] G.H. Döhler, H. Klüngel, D. Olego, K. Ploog, P. Ruden, H.J. Stolz, and G. Abstreiter, Phys. Rev. Lett. **47**, 864 (1981).
[20] E.F. Schubert, T.D. Harris, and J.E. Cunningham, Appl. Phys. Lett. **53**, 2208 (1988).
[21] K. Ploog, A. Fischer, and H. Kunzel, J. Electrochem. Soc. **128**, 400 (1981).
[22] P.M. Koenraad and M.B. Johnson, Inst. Phys. Conf. Ser. **156**, 245 (1998).